geosciences

MDPI

Article

Numerical Study of Mechanical Behavior and Fracture Characteristics of Dolomitic Limestone with Densely Distributed Small Holes

Shuai Yuan [1], Xianfeng Wang [1], Qinghai Sun [1], Zhiguo Wang [2], Guantao Tai [3,*], Guangyao Zhang [2] and Shuai Liu [4,*]

[1] Henan Provincial Land and Spatial Survey and Planning Institute, Zhengzhou 450016, China
[2] School of Civil Engineering and Transportation, North China University of Water Resources and Electric Power, Zhengzhou 450046, China
[3] Henan No. 5 Geological Brigade Co., Ltd., Zhengzhou 450018, China
[4] Henan Key Laboratory of Geomechanics and Structural Engineering, North China University of Water Resources and Electric Power, Zhengzhou 450046, China
* Correspondence: taigt1990@163.com (G.T.); liushuai1@ncwu.edu.cn (S.L.)

Abstract

Densely distributed small holes significantly affect the mechanical behavior and fracture characteristics of rock masses. In this study, the two-dimensional particle flow code was employed to establish a series of numerical models of dolomitic limestone, with the number of small circular holes increasing according to the sequence $(2n-1)^2$ (n = 1–6). Comparative models with equivalent area and variable spacing were additionally designed to explore their regulatory effects. The strength, crack evolution, and contact force chain distribution of each model were systematically analyzed. The results reveal that the number of small holes exhibits an approximately linear negative correlation with the rock strength. The number of holes dominates the crack initiation location and propagation path. The crack initiation stress gradually decreases with increasing hole number, while the ratio of crack initiation stress to peak stress exhibits a V-shaped trend. As the hole number increases, the distribution of compressive force chains shifts from the sides of holes to the vertical strips between holes, and tensile force chains become significantly enhanced in the areas above and below the holes. Hole spacing and equivalent area exert only local modulating effects; the number and spatial arrangement of holes remain the dominant controls on strength deterioration and fracture evolution. These findings offer a theoretical foundation for stability assessment in rock masses characterized by densely distributed hole defects.

Keywords: densely distributed holes; dolomitic limestone; mechanical behavior; fracture characteristics; PFC2D; equivalent area

Check for updates

Academic Editor: Pinnaduwa Kulatilake

Received: 29 May 2026
Revised: 12 July 2026
Accepted: 16 July 2026
Published: 19 July 2026

Copyright: © 2026 by the authors. Licensee MDPI, Basel, Switzerland. This article is an open access article distributed under the terms and conditions of the Creative Commons Attribution (CC BY) license.

1. Introduction

Natural rock masses commonly contain various defects, including holes and fissures, which contribute to marked heterogeneity, discontinuity, and anisotropy in their physical and mechanical properties [1–3]. Such features are particularly prevalent in vesicular igneous rocks (e.g., basalt and zeolite) and in soluble carbonate rocks (e.g., limestone and dolomite) that have undergone dissolution, where relatively dense concentrations of small-scale hole defects are frequently observed (Figure 1). These randomly distributed small holes, present in large quantities, further complicate the mechanical behavior of the rock mass, including its physical properties, deformation, and fracturing. When such a rock

mass containing numerous small holes serves as an engineering rock mass, it significantly increases the difficulty of engineering design and construction, posing a serious threat to construction safety [4,5]. Therefore, investigating the influence of a large number of small holes on the macro- and mesoscopic failure mechanisms and mechanical properties of rock masses is both necessary and of considerable scientific and engineering significance.

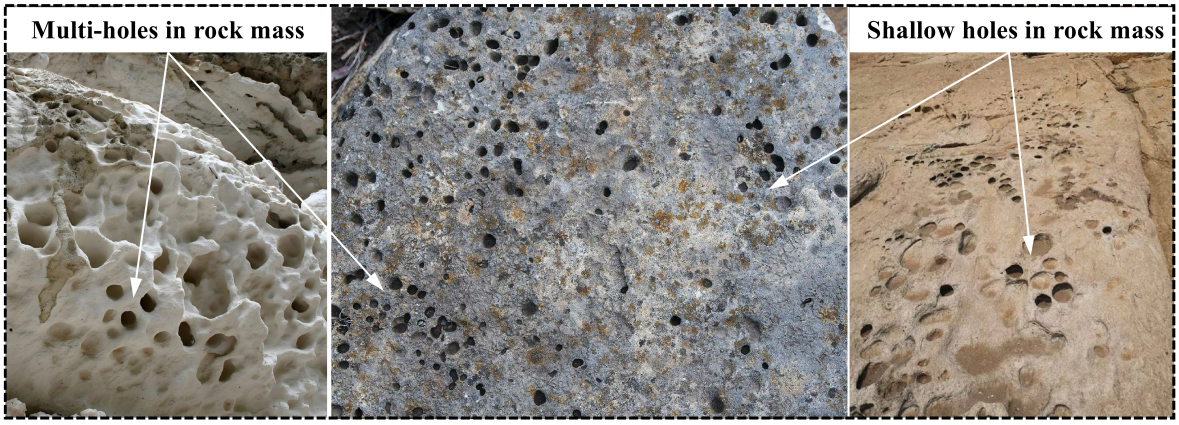


Figure 1. Densely distributed small holes developed in rock masses.

The mechanical behavior of rock masses containing hole-type defects has attracted sustained research interest in rock mechanics and allied disciplines over recent decades. A substantial body of literature has addressed the macro- and mesoscopic mechanical responses of rock specimens containing isolated regular holes, as well as those with two or more interacting holes, yielding a wealth of experimental and numerical findings [6,7]. Studies concerning single-hole configurations are particularly numerous, with the primary research focuses encompassing the influences of hole geometry [8], size [9], spatial position [10], and the presence of infill materials or reinforcement [11] on the macroscopic mechanical response. For instance, Lin et al. [12] and Xia et al. [13] conducted experimental and numerical simulation analyses on rock specimens containing a single hole defect of various shapes (e.g., circular, square), analyzing the controlling effect of hole shape on rock deformation and failure. Liu et al. [14] and Cui et al. [15] analyzed the variations in mechanical strength and failure modes of rock masses containing circular or spherical hole defects of different sizes, investigating the deterioration mechanism of mechanical properties due to the size effect of a single hole. Regarding combinations of two or more holes, or combinations of holes with other defect types such as fissures, current research is most abundant, primarily focusing on variables such as the number, distribution, and arrangement of circular holes and other defect combinations [16,17]. For example, Ma et al. [18] and Du et al. [19] conducted compression tests and numerical simulations on rock or rock-like specimens with two circular holes, investigating the effects of inclination angle and filling conditions on strength, failure mode, and crack evolution behavior. Huang et al. [20] performed experimental and simulation analyses on granite specimens containing three non-coplanar holes, focusing on the damage and failure mechanisms under the influence of the three holes. Liu et al. [21] used the two-dimensional Particle Flow Code (PFC2D) to analyze the influence of two and three circular holes, along with variations in spacing and inclination, on rock mass damage and fracture characteristics. Tang et al. [22] conducted numerical experiments on heterogeneous brittle solids containing single, three, and hole-like defects to reveal the mechanisms of splitting failure observed in brittle solids. Huang et al., Li et al., Yue et al., and Han et al. [23–26] established combined defect models incorporating both holes and fissures, conducting laboratory experiments and numerical simulations to study the strength, failure modes, and crack propagation evolution of rock

masses with such combined defects. It is evident that when multiple or various types of hole defects interact, the damage and deformation failure mechanisms of the rock mass become significantly more complex. Some scholars have also investigated the mechanical properties of rock masses containing a relatively large number of small hole defects (greater than three in quantity) [27]. Others have defined "porous rock mass" from the perspective of high porosity, primarily analyzing the influence of porosity on strength and permeability characteristics [28,29]. For instance, Huang et al. [30] conducted laboratory experiments and particle flow discrete element simulations on granite specimens containing multiple small holes to study the fracture characteristics and failure modes under the influence of multiple small holes. Gui et al. [31] used numerical simulation and laboratory experiments to analyze crack development and failure mechanisms in rock specimens with various arrangements of multiple small circular holes. Al-Harthi et al. [32] and Bubeck et al. [33] analyzed the influence of porosity and hole shape on the mechanical properties of vesicular basalt. Heap et al. [34] and Griffiths et al. [35] employed numerical simulation methods to explore the weakening mechanism of hole structure parameters on rock strength and their influence on rock anisotropy. Concurrently, these studies also demonstrate that with the rapid development of computer technology and numerical simulation methods, various numerical simulation techniques have been widely applied in rock mechanics research, with mesoscopic simulation methods playing a crucial role in analyzing the mechanical behavior of heterogeneous materials, particularly rock masses containing hole defects [36–38].

Most of the aforementioned studies on rock masses with hole defects focus on the influence of a limited number of holes on mechanical properties, with studies on densely distributed small holes often included for comparative analysis. The mesoscopic mechanical characteristics of rock masses with numerous densely distributed hole defects require further investigation, particularly the evolution patterns of mechanical strength and crack propagation with variations in the number of holes and equivalent area. Motivated by the densely distributed cavity pattern observed in Figure 1, the present study focuses on dolomitic limestone, which is characterized by abundant small dissolution cavities, as the subject of investigation. Using the two-dimensional particle flow code (PFC2D), a series of numerical simulations is performed to examine the strength, failure behavior, and fracture characteristics of this material under uniaxial compression.

2. Numerical Models and Parameter Determination

2.1. Determination of Numerical Simulation Parameters

Using PFC2D numerical simulation for rock mechanics tests is an effective method for studying macroscopic mechanical problems from a mesoscopic perspective. Compared with macroscopic laboratory tests, the parallel bond model (PBM) in the PFC code can effectively simulate particle interactions, deformation, and fracturing, making it highly suitable for analyzing mesoscopic characteristics during the progressive failure process of rocks [39–41]. To calibrate and determine the parameters used in this simulation, laboratory uniaxial compression tests were first conducted on rock samples to measure their basic physical and mechanical parameters. The rock samples were dolomitic limestone, prone to containing small dissolution holes, prepared as standard cylindrical specimens with a height-to-diameter ratio of 2:1 (100 mm × 50 mm). The tests were performed using a YAW6206 computer-controlled electro-hydraulic servo pressure testing machine (MTS Industrial Systems (China) Co., Ltd., Shanghai, China) under deformation control, with a loading rate set to 0.001 mm/s. The testing apparatus and rock samples are shown in Figure 2. The basic physical and mechanical parameters obtained for the dolomitic limestone are presented in Table 1.

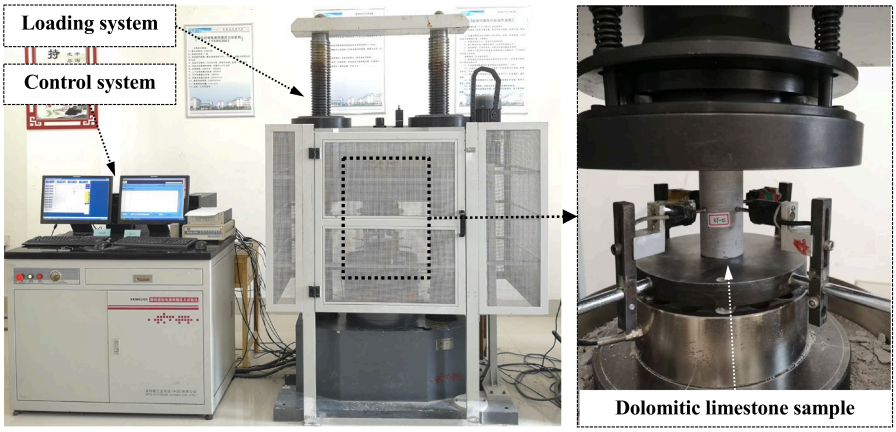


Figure 2. Testing apparatus and dolomitic limestone specimens.

Table 1. Basic physical and mechanical parameters of dolomitic limestone material.

Parameters	Density (kg/m^3)	Uniaxial Compressive Strength (MPa)	Uniaxial Tensile Strength (MPa)	Elastic Modulus (GPa)	Cohesive Force (MPa)	Internal Friction Angle (°)
Dolomitic limestone	2740	123.49	10.32	76.60	16.29	42.5

Using the experimentally determined mechanical properties of dolomitic limestone as a reference, the numerical stress–strain response obtained from PFC2D simulations under equivalent loading conditions was matched against the laboratory measurements. Through this calibration process, a set of microscopic parameters appropriate for the PFC2D model was established. The resulting uniaxial compression stress–strain curves and failure modes from the experiment and numerical simulation are compared in Figure 3. It is worth noting that the stress–strain curves derived from the numerical simulations do not show a compaction stage, which is attributed to the rigid-body assumption for rock particles in the PFC2D model. It can be observed that while slight discrepancies exist in the peak strain (displacement) between the experimental and numerical specimens, the peak strength and deformation modulus are generally consistent. The calculated relative errors for peak stress and elastic modulus are 0.44% and 0.67%, respectively, indicating good agreement between the numerical model and laboratory measurements. This demonstrates that the calibrated microscopic parameters of the PFC model satisfy the requirements of the simulation tests. The microscopic mechanical parameters for the limestone and joints based on PFC are listed in Table 2.

Table 2. Microscopic parameters of limestone and joint material.

Parameters	Rock Block (Value) Dolomitic Limestone
Minimum particle diameter (mm)	0.20
Particle diameter ratio	1.50
Grain density (kg/m^3)	3044
Contact modulus of the particle (GPa)	36.21
Contact bond gap (mm)	0.05
Coefficient of friction	0.60
Porosity	0.10
Parallel bond friction angle (°)	42.5
Parallel bond tensile strength (MPa)	10.95
Normal critical damping ratio	0.50
Parallel bond cohesive force (MPa)	52.23

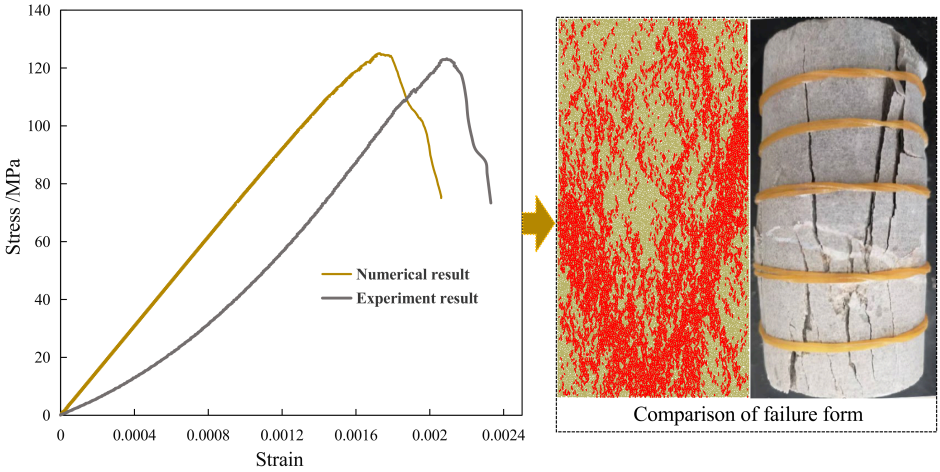


Figure 3. Comparison of experimental and numerical simulation calibration results.

2.2. Numerical Model Establishment

To better investigate the influence of densely distributed small holes on the mechanical properties of the rock mass, the numerical model was established as a square with dimensions of 100 mm × 100 mm. The square shape was adopted to provide a well-balanced geometry that minimizes potential boundary effects under various hole configurations, while the 100 mm height preserves the same vertical dimension as the physical specimens. This two-dimensional representation follows the conventional plane-strain assumption commonly employed in numerical studies of rock mechanics, allowing for a reasonable qualitative comparison between the simulated and experimental results. For model construction in PFC2D, the parallel bond model was employed as the contact constitutive model, as it enables the transmission of both forces and moments between particles. A particle assembly with radii ranging from 0.20 to 0.30 mm was randomly generated within a 100 mm × 100 mm domain. Subsequently, the expansion method was adopted to achieve a target porosity of 0.1 for the numerical models [42]. The small holes were modeled as common circles with a diameter of 5 mm. The number of small holes was set according to Equation (1), uniformly distributed within the model centered on the model's center point, with the distance between holes also set to 5 mm. Consequently, the number of holes was 1^2, 3^2, 5^2, 7^2, 9^2, and 11^2. The established numerical models are shown in Figure 4, named A1, A2, A3, A4, A5, and A6, respectively. All numerical models were established under identical boundary conditions. In model A6, the outermost holes are exposed on the rock surface, resulting in semicircular hole shapes. The distribution of small holes in models A5 and A6 creates a "honeycomb-like" morphology. It should be noted that the microscopic inter-particle porosity in the PFC2D model is determined by the particle size distribution and compaction process, and remains essentially constant across all model configurations. The macroscopic holes introduced in this study are created by removing particles within specified regions and are treated as structural defects at the specimen scale. Furthermore, to systematically evaluate the influences of equivalent area and variable spacing of small holes on the mechanical behavior of the rock specimens, comparative model series with varying equivalent hole areas and adjacent hole spacings were designed in addition to the baseline models presented in Figure 4. A detailed analysis and interpretation of the regulatory effects of equivalent area and hole spacing are provided in the Section 4.

$$A_n = (2n-1)^2,\ (n = 1,\ 2,\ 3,\ \cdots) \tag{1}$$

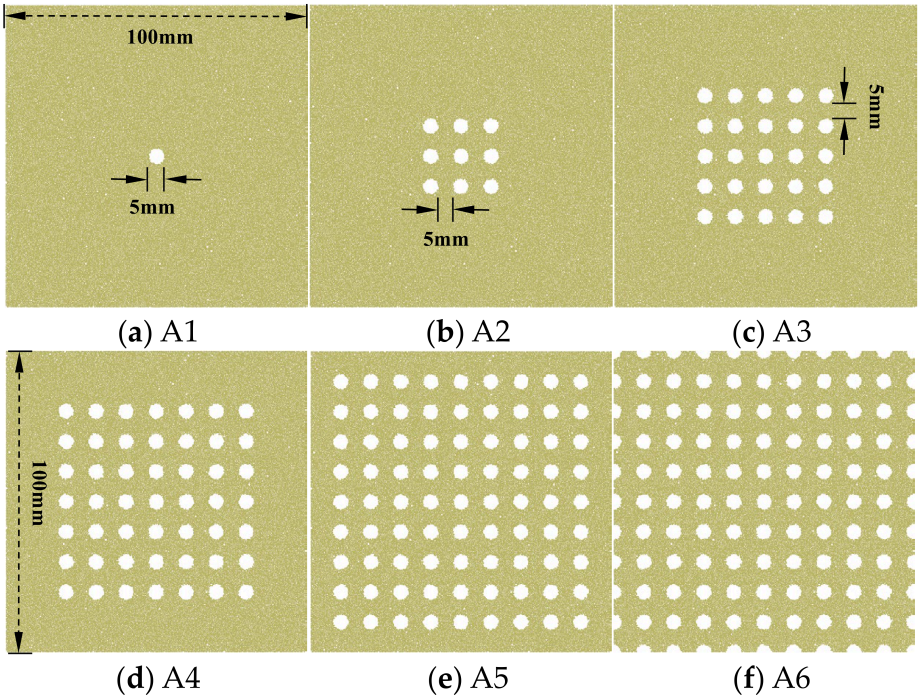


Figure 4. Numerical models.

In the parallel bond model within the PFC code, the spatial distribution of particles differs for each PFC model, potentially leading to slight variations in the simulated stress–strain response. Therefore, to ensure the accuracy and reliability of the mesoscopic parameters, a stochastic analysis of the mesoscopic parameters for dolomitic limestone is necessary [11,43,44]. During the calibration process of the numerical model parameters in this study, the random seed was set to 1×10^4. To verify the reliability and applicability of the mesoscopic parameter set in the PFC code, a complete numerical model without holes (100 mm × 100 mm) was established and re-analyzed. Using the same mesoscopic parameters, simulations were rerun with random seeds set to 1×10^4, 2×10^4, and 3×10^4. The resulting peak stress and elastic modulus values for the square intact model under different random seeds are shown in Table 3. The crack evolution patterns at the post-peak stage (70% of peak stress), representing the failure morphology, are shown in Figure 5. It can be observed that under different random seeds, the peak stress and elastic modulus values of the square intact dolomitic limestone models are essentially equivalent, and the failure modes are similar, indicating that the calibrated mesoscopic parameters are reliable.

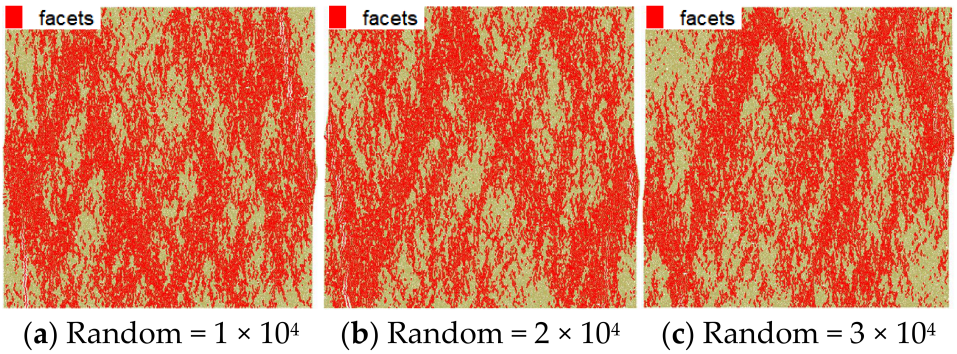


Figure 5. Numerical models for different random seeds.

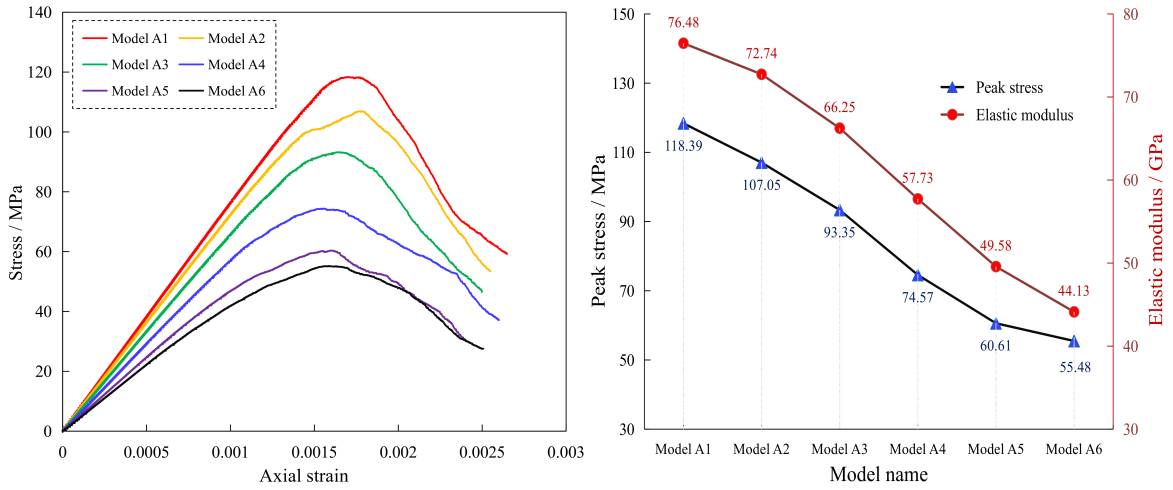
Table 3. Peak stress and elastic modulus values under different random seeds.

Mechanical Parameters	Random = 1 × 10^4	Random = 2 × 10^4	Random = 3 × 10^4
Peak stress (MPa)	123.50	124.03	123.47
Elastic modulus (GPa)	76.62	76.68	76.62

3. Analysis of Numerical Simulation Results

3.1. Analysis of Stress–Strain Characteristics of Each Model

The stress–strain curves for each model are shown in Figure 6a, while the mechanical characteristic curves for peak strength and elastic modulus are presented in Figure 6b.



(**a**) Stress–strain curve (**b**) Elastic modulus and peak stress

Figure 6. Stress–strain, elastic modulus and peak stress variation curves of each model.

As illustrated in Figure 6, Model A1 yields the highest values of both peak stress and elastic modulus, whereas Model A6 registers the lowest. The peak stresses for Models A1 to A6 are 118.39 MPa, 107.05 MPa, 93.35 MPa, 74.57 MPa, 60.61 MPa, and 55.48 MPa, respectively. Compared to the peak stress of the intact model (123.50 MPa), these represent decreases of approximately 4.14%, 13.32%, 24.41%, 39.62%, 50.93%, and 55.08%. The elastic moduli for Models A1 to A6 are 76.48 GPa, 72.74 GPa, 66.25 GPa, 57.73 GPa, 49.58 GPa, and 44.13 GPa, respectively. Compared to the elastic modulus of the intact model (76.62 GPa), these represent decreases of approximately 0.18%, 5.06%, 13.54%, 24.65%, 35.29%, and 42.40%. The results clearly demonstrate that as the number of small holes increases following the progression defined by Equation (1), both the peak stress and the elastic modulus of the specimens decline monotonically. This relationship can be characterized as an approximately linear negative correlation between the count of uniformly distributed small holes and the overall mechanical strength of the rock mass.

3.2. Analysis of Crack Development and Evolution Characteristics of Each Model

Using the peak stress of each model as a reference, and considering crack initiation characteristics and stress levels, stress levels corresponding to 30%, 70%, and 100% of the peak stress and 70% of the peak stress in the post-peak stage (failure morphology) were selected to analyze the evolution characteristics of crack initiation, propagation, and coalescence within each model. The crack development and evolution within each rock specimen are shown in Figure 7, where the rock specimen background is set to yellowish-brown, black cracks represent shear cracks, and red cracks represent tensile cracks.

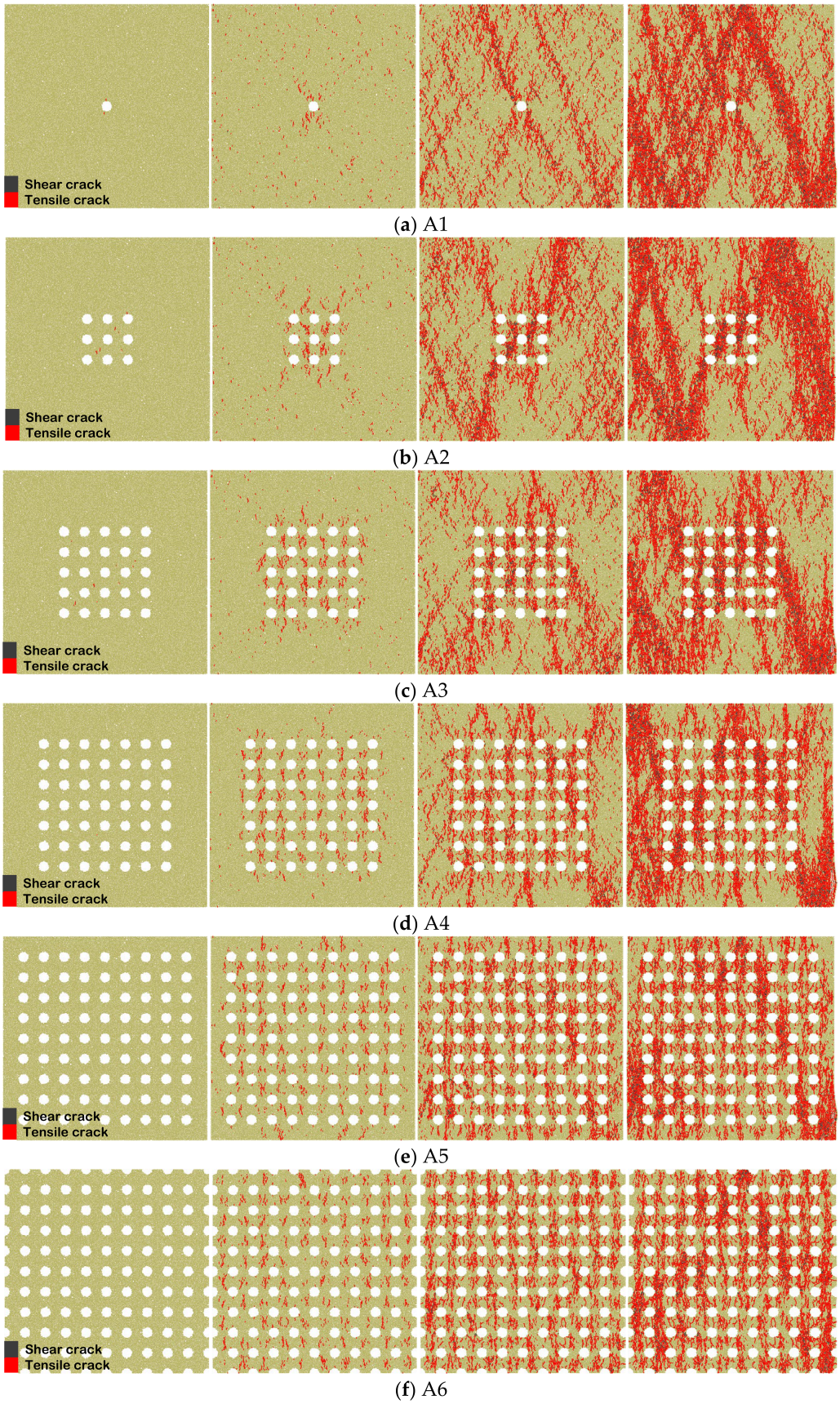


Figure 7. Crack development and evolution characteristics in each model.

Figure 7 illustrates that as the applied stress level increases, crack development in all models proceeds through four distinct stages: an initial stage with no cracking, followed

by crack initiation, then slow propagation, and finally rapid crack growth. At the 30% peak stress loading stage, in Model A1, microcracks only initiate near the top and bottom points of the small hole, with no crack initiation observed elsewhere. In Models A2 and A3, a small number of microcracks initiate mainly between the small holes. In Model A4, only one microcrack initiates between the small holes, while no crack initiation occurs in Models A5 and A6. This observation suggests that the number of small holes exerts a controlling influence on both the onset of microcracking and the spatial location where cracks first appear. To better analyze the crack initiation stress characteristics and crack types in each model, the stress characteristic values at crack initiation and the crack types were recorded, yielding the crack initiation stress values shown in Table 4. The crack initiation stresses for Models A1 to A6 are approximately 28.85 MPa, 25.71 MPa, 22.40 MPa, 21.76 MPa, 20.05 MPa, and 18.62 MPa, respectively, showing an overall decreasing trend consistent with the variation trend of peak stress. It is noteworthy that the ratio of crack initiation stress to peak stress exhibits a V-shaped trend, decreasing from Model A1 to A3 and then increasing from Model A4 to A6. This trend can be explained by the differential rates of decline between crack initiation stress and peak stress. From Models A1 to A3, crack initiation stress declines more rapidly than peak stress because the increasing number of holes introduces more stress concentration sites that facilitate earlier cracking, while the peak stress is still largely sustained by the relatively intact rock matrix. From Models A4 to A6, however, the peak stress declines more rapidly than crack initiation stress. This is because when the number of holes becomes sufficiently large, the overlapping stress disturbance zones between adjacent holes substantially compromise the overall structural integrity of the specimen, leading to a pronounced reduction in peak strength. Meanwhile, crack initiation remains a locally controlled phenomenon governed by the maximum tensile stress at individual hole boundaries, which becomes less sensitive to further increases in hole number once a critical density is exceeded. In the "honeycomb-like" configurations of Models A5 and A6, the limited rock bridges between adjacent holes further accelerate the degradation of peak stress relative to crack initiation stress, resulting in an increasing ratio.

Table 4. Crack initiation stresses and crack types for each model.

Model Name	Crack Initiation Stresses (Mpa)	Crack Type	Percentage of Peak Stress (%)
A1	28.85	Tensile	24.37
A2	25.71	Tensile	24.02
A3	22.40	Tensile	23.40
A4	21.76	Tensile	29.18
A5	20.05	Tensile	33.08
A6	18.62	Tensile	33.56

Upon further compression to 70% peak stress, cracks in each model continue to propagate near the small holes, with microcracks still predominantly concentrated within and around the small hole areas, while fewer cracks are generated in the outer regions without holes. This suggests that as the number and distribution range of small holes increase, the crack propagation zone also expands. When loaded to the peak stress, each model is in a critical failure state, with a large number of cracks developing and coalescing, forming coalesced failure cracks within the models. In Models A1 to A4, the degree of crack coalescence is high, resulting in several distinct main failure cracks. In contrast, in Models A5 and A6 with their "honeycomb-like" morphology, the paths for crack propagation are limited to the rock bridges between the small holes, leading to poor crack coalescence and less distinct main failure cracks in these models. At the post-peak stage (70% of peak stress), the number of cracks developed in each model reaches a maximum. The total number

of cracks, along with the number of tensile and shear cracks for each model, is shown in Figure 8. It can be seen that the total number of cracks, as well as the number of tensile and shear cracks, decreases progressively with the increase in the number of small holes. After model failure, the concentrated areas of tensile and compressive cracks represent the failure morphology of each model, and the crack count can indicate the degree of fragmentation. Notably, the progressive decrease in total crack count from Models A1 to A6 should not be interpreted as an indication of less severe damage. Rather, this reduction is attributable to the increasing proportion of the specimen area occupied by macroscopic holes as the hole number increases, which correspondingly diminishes the available volume of rupturable material for crack initiation and propagation. To provide a more rigorous characterization of the failure extent, the crack density was defined as the number of cracks per unit area of rupturable material (i.e., the model area excluding the regions occupied by holes). While the absolute number of cracks exhibits a monotonic decrease from models A1 to A6, the crack density reveals a distinct increasing trend. In the "honeycomb-like" configurations of Models A5 and A6, cracks are preferentially concentrated within the limited rock bridges between adjacent holes. This indicates a higher degree of localized damage and more pronounced structural degradation.

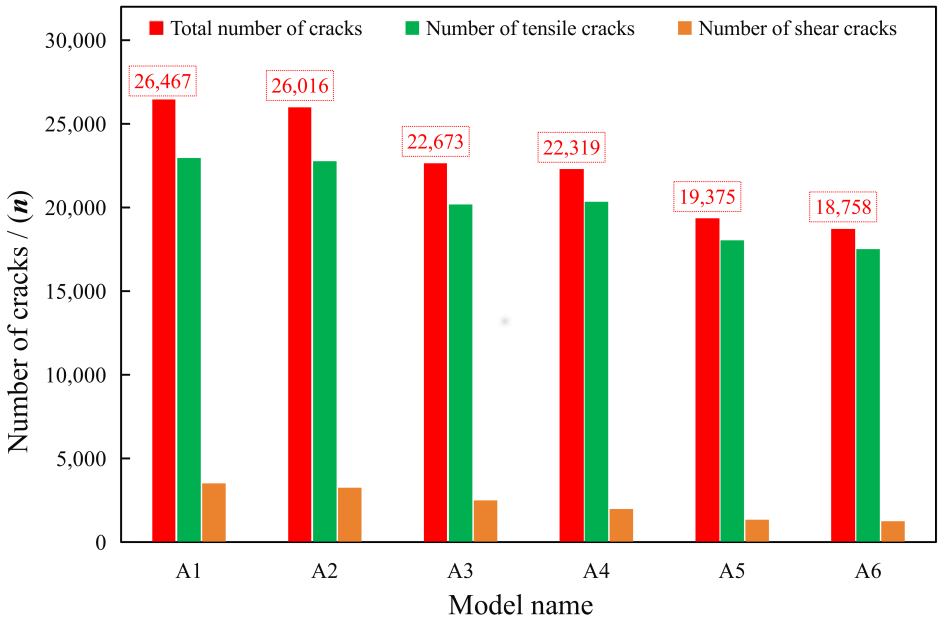


Figure 8. The histogram of crack number of each model in failure stage.

3.3. Analysis of Contact Force Chain Distribution Characteristics of Each Model

Using the peak stress of each model as a reference, the distribution characteristics of contact force chains were analyzed at stress levels corresponding to 70% peak stress, peak stress, and 70% peak stress in the post-peak stage. The distribution characteristics of contact force chains for each model are shown in Figure 9. In the contact force chain diagrams, dark red force chains represent compressive stress, blue force chains represent tensile stress, and the model background is indicated in light yellowish-brown. Denser force chains in the parallel contact force distribution diagrams, represented by darker colors in Figure 8, indicate a higher degree of stress concentration.

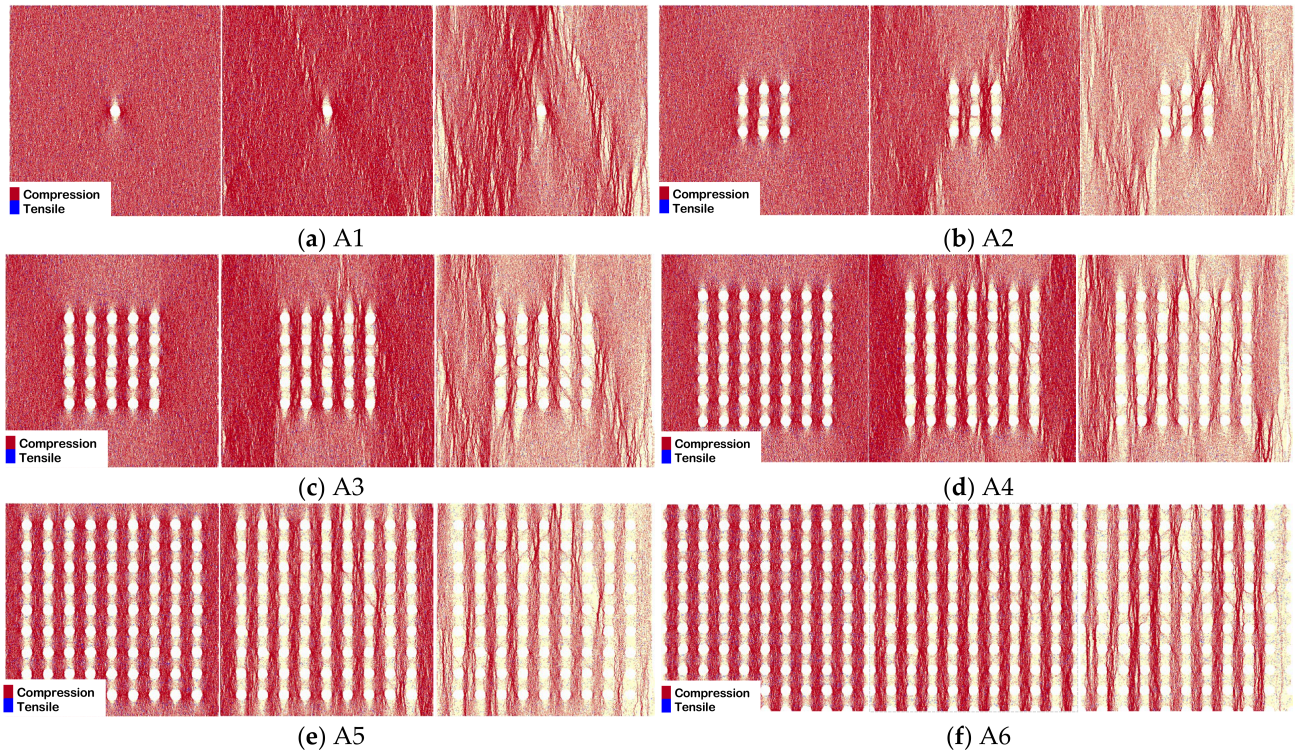


Figure 9. Distribution and evolution characteristics of contact force chains in each model.

At the 70% peak stress loading level (Figure 9), the compressive force chains in Model A1 exhibit only a slight densification on the lateral flanks of the hole, with a relatively uniform distribution prevailing throughout the remainder of the specimen. Tensile force chains are dispersedly distributed as spots in the model, slightly more pronounced near the top and bottom of the small hole, which is consistent with the crack propagation primarily occurring near the small hole at this stage. In Models A2 to A5, compressive force chains are denser between the left and right sides of the small holes, while they are relatively sparse in the areas near the top and bottom vertices of the holes and in the regions extending vertically from the entire hole area to the model boundaries. In these areas, tensile force chains are relatively denser. This indicates that compressive stress is partially released in the regions extending vertically from the hole area to the model boundaries, while compressive force chains are densely distributed vertically between the model sides and the holes. In Model A6, due to the release of compressive stress near the top and bottom vertices of the holes, distinct vertical band-like dense distributions of compressive force chains are formed, while tensile force chains are relatively more prominent between individual holes. At the peak stress level, each model is in a critical failure state. In Model A1, an inclined zone of sparse compressive force chains develops along the hole. In Model A2, distinct compressive stress release zones appear near the areas above and below the small holes and along the diagonal directions, with compressive force chains forming dense zones on both sides of the model and on both sides of the central column of holes. Similarly, in Models A3 and A4, compressive force chains are mainly concentrated on both sides of the model and between the vertical columns of holes, forming distinct vertically aligned dense zones of compressive force chains. The areas extending vertically from the hole regions are primarily stress release zones, where the main failure occurs. In Models A5 and A6, the compressive force chains between vertically aligned holes are even more concentrated, forming vertical band-like compressive force chain concentration zones that bear the majority of the compressive stress. In the post-peak stage, the distributions of compressive and tensile force chains in all models are relatively sparser compared to those

at peak stress, indicating that the contact force chains have been released, although some concentrated areas still bear the loading. The main stress release zones appearing in each model are consistent with the crack propagation zones shown in Figure 6. In summary, the number of small holes governs the spatial distribution of contact force chains within the rock specimen, thereby altering both the locations and the orientations of compressive and tensile stress concentrations.

4. Discussion

The present work utilizes the PFC2D discrete element method to explore how densely distributed small cavities regulate the mechanical response and fracture behavior of dolomitic limestone. A series of numerical models was generated with the cavity count progressively increasing in accordance with Equation (1), enabling the identification of intrinsic links between the number and spatial density of holes and the macroscopic mechanical behavior of the rock. The results show that an increase in the number of small holes significantly deteriorates the strength and elastic modulus of the rock mass, while altering crack initiation locations, propagation paths, contact force chain distributions, and the final failure mode. These findings are generally consistent with the results of related studies [20–22] concerning the influence of multiple holes on rock mass mechanical behavior. Currently, research on the mechanical properties of "honeycomb-like" rock masses containing densely distributed small holes is relatively limited. In designing the numerical models for rock masses with multiple densely distributed small holes, this study primarily considered the number of small holes as a variable, while fixing the spacing between holes at 5 mm. However, relevant literature [45–47] also suggests that hole spacing and equivalent hole area influence the mechanical properties and behavior of rock masses.

To further elucidate the respective roles of equivalent hole area and inter-hole spacing, Model A3 (containing 25 holes with 5 mm spacing) was selected as the reference configuration. Five additional models, designated A3-1 through A3-5, were subsequently established for comparative purposes. In A3-1, the 25 small holes were combined into a single large hole with a diameter of 25 mm to investigate the differential effects of hole number and morphology under the same equivalent area. Models A3-2 to A3-5 were configured with hole spacings of 0 mm, 1 mm, 10 mm, and 15 mm, respectively, to reveal the regulatory effect of hole spacing on mechanical properties. The five comparison models are shown in Figure 10. The variation trends of mechanical strength and elastic modulus for each comparison model are shown in Figure 11. A comparative analysis of crack initiation, propagation, and coalescence characteristics for each model was also performed at 30%, 70%, and 100% of the peak stress, as shown in Figure 12.

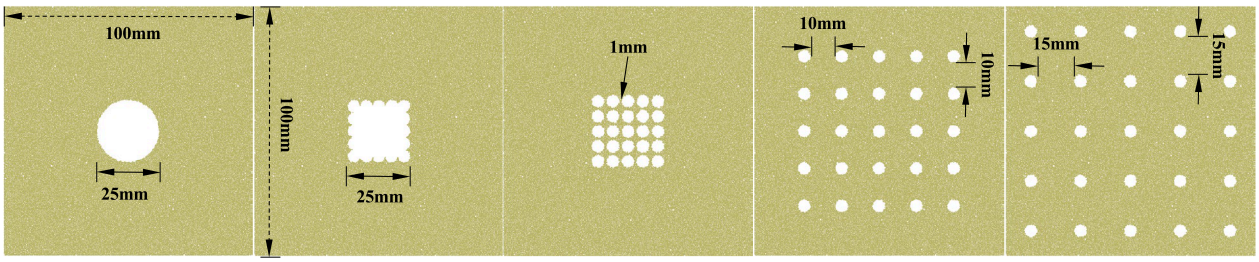


Figure 10. Numerical models for comparison and validation.

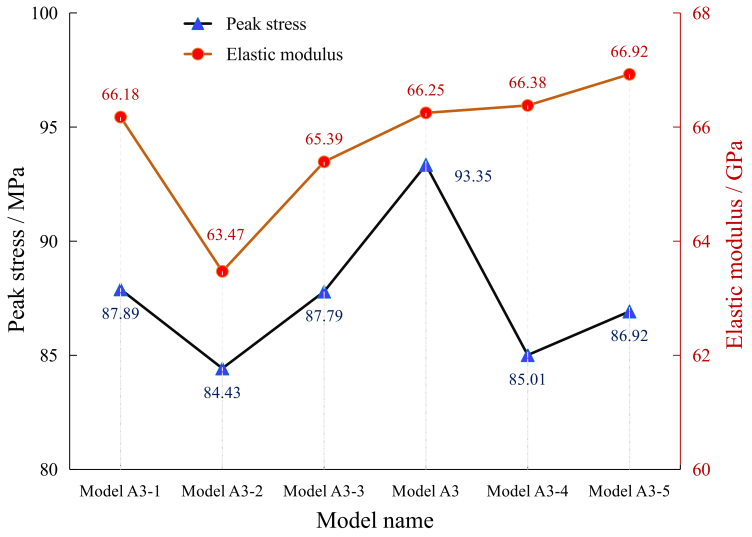


Figure 11. Peak stress and elastic modulus of comparison numerical models.

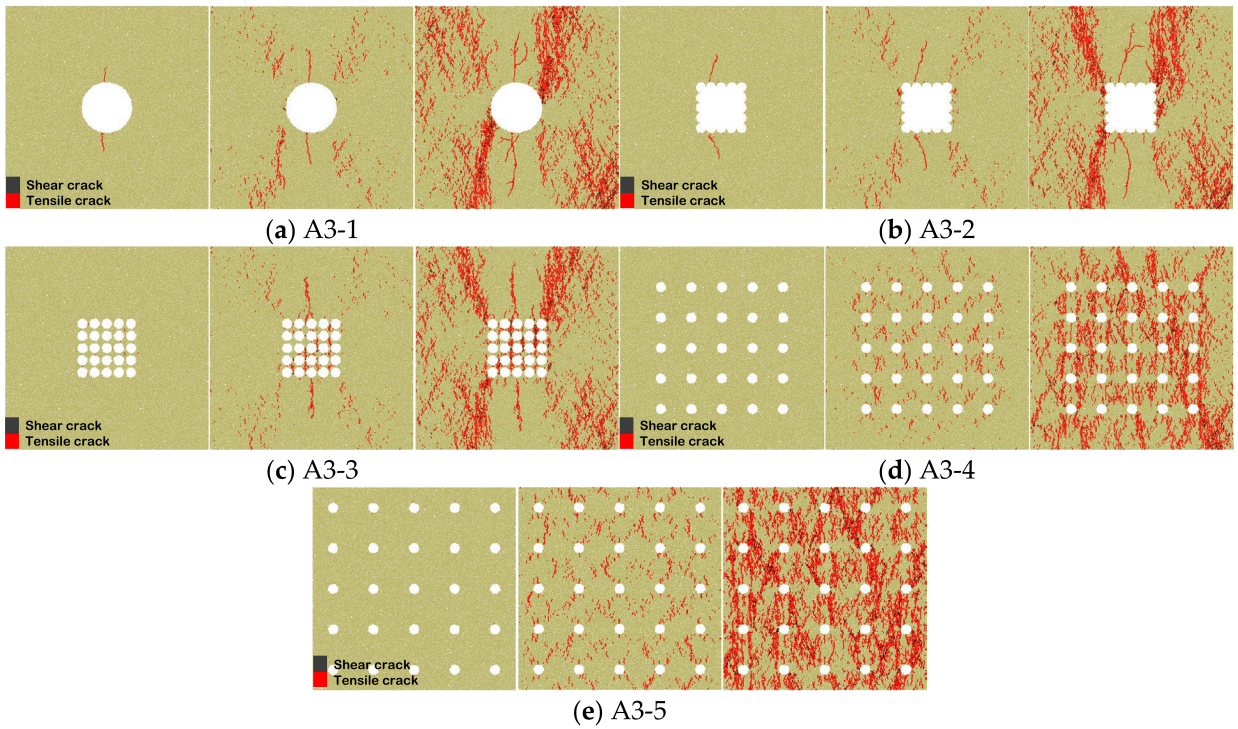


Figure 12. Comparison and validation of numerical models.

As shown in Figure 11, Model A3-2, with zero hole spacing leading to particle loss between holes and a relatively larger equivalent area, exhibits the lowest peak stress and elastic modulus, at 84.43 MPa and 63.47 GPa, respectively. In comparison, Model A3-5 (spacing 15 mm) has the highest elastic modulus (66.92 GPa), but its peak strength is slightly lower than that of Model A3. Among all models, Model A3 still exhibits the highest peak stress (93.35 MPa), indicating that appropriately increasing hole spacing helps improve specimen stiffness but has a limited effect on enhancing strength. Except for A3-2, the differences between the maximum and minimum values of peak stress and elastic modulus among the other comparison models are 8.34 MPa and 1.53 GPa, respectively. Specifically, the peak stress varies from 85.01 MPa to 93.35 MPa, and the elastic modulus ranges from 65.39 GPa to 66.92 GPa, among these models. This comparison suggests that both the equivalent area and spacing of small holes moderately influence

the macroscopic mechanical response of the rock mass. When hole spacing is relatively large or the equivalent area is similar, the differences in macroscopic mechanical response among specimens are minor, and the number of holes and their spatial arrangement have a more significant influence on mechanical properties. It is worth noting that the equivalent-area concept provides a first-order framework for distinguishing the effects of hole number from those of total void area. Nevertheless, its limitations should be recognized. First, holes with the same total area are not mechanically equivalent, as individual hole size governs local stress concentration. Second, the spatial distribution of holes, a key factor controlling their interaction, is not accounted for in this comparison. Third, the 2D equivalent-area metric does not directly correspond to volumetric void fractions in 3D. Consequently, the equivalent-area analysis offers qualitative trends rather than strictly quantified relationships.

Regarding crack evolution characteristics (Figures 7 and 12), when only a single hole exists in the model, regardless of its size, cracks preferentially initiate at the top and bottom endpoints of the hole and propagate steadily along the loading direction, exhibiting a typical tensile failure mode. As the number of holes increases, the top and bottom endpoints of each hole become stress concentration zones, with cracks initiating, propagating, and coalescing within the rock bridge areas between adjacent holes, forming a complex crack network. A greater number and wider distribution of holes lead to a higher degree of crack coalescence and an expanded failure zone, resulting in a more fragmented final failure morphology. Notably, in "honeycomb-like" structures such as Models A5 and A6, the dense distribution of holes restricts crack propagation paths to the narrow rock bridges between holes. Cracks struggle to form penetrating main failure surfaces, resulting in a lower total crack count. However, local stress concentration intensifies, and the load-bearing capacity deteriorates further. This phenomenon suggests that when hole density exceeds a certain threshold, the failure mechanism of the rock mass gradually transitions from brittle failure dominated by macroscopic cracks to progressive failure controlled by local fragmentation.

In summary, the number of small holes, their equivalent area, and their spacing collectively constitute key factors influencing the macro- and mesoscopic mechanical behavior of the rock mass. Among these, the number of holes has the most significant controlling effect on strength deterioration and crack evolution, while hole spacing and equivalent area exert localized regulatory effects on mechanical properties under specific conditions. The model of densely distributed small holes constructed in this study effectively characterizes the mechanical response of "honeycomb-like" rock masses. The research findings hold significant theoretical value and engineering guidance for the stability evaluation and disaster prevention and control in rock mass engineering containing densely distributed hole defects, such as areas with developed dissolution features or zones with vesicular igneous rocks. Future research will extend the current investigation to triaxial compression conditions, exploring the effects of varying confining pressures on the mechanical behavior and failure mechanisms of densely hole-bearing rock masses. This will enhance the practical relevance of our findings for deep underground engineering applications.

5. Conclusions

Based on the PFC2D discrete element numerical simulation method, this study investigated the mechanical behavior and mesoscopic fracture characteristics of various models approximating a "honeycomb-like" structure, using dolomitic limestone with densely distributed small holes as the research object. The main conclusions are as follows:

(1) The number of uniformly distributed small holes exhibits an approximately linear negative correlation with the mechanical strength of the rock mass. As the number of small holes progressively increases, both the peak stress and elastic modulus of the

rock specimens exhibit a decreasing trend, indicating that the number of holes is the dominant factor controlling the deterioration of rock mass strength.

(2) The number of small holes plays a decisive role in crack initiation behavior, location, and propagation paths. With an increasing number of holes, the crack initiation location in the model gradually extends from the hole endpoints to the rock bridge areas between holes. The crack initiation stress exhibits an overall decreasing trend, while the ratio of crack initiation stress to peak stress shows a V-shaped trend of first decreasing and then increasing. The total number of cracks, as well as the number of tensile and shear cracks, decreases progressively with the increase in the number of small holes. This reflects the characteristics of limited crack propagation space and concentrated fracturing under densely distributed hole conditions. To some extent, it also indicates that as the number of holes increases, the number of newly generated cracks during post-peak failure decreases, making the model relatively more prone to failure and resulting in a greater degree of fragmentation.

(3) An increase in the number of holes leads to the migration and redistribution of stress concentration zones within the model and also alters the distribution characteristics of contact force chains. Compressive force chains gradually concentrate from the sides of the holes to the vertical band-like zones between the holes, while tensile force chains become significantly enhanced in the areas extending vertically from the holes, forming distinct stress release zones that subsequently govern the direction of crack initiation and propagation.

(4) The equivalent area of small holes and the hole spacing exert localized regulatory effects on the macro- and mesoscopic mechanical behavior of the rock mass. Under conditions of varying hole spacing or equivalent area, the number of holes and their spatial arrangement exhibit the most significant controlling effect on the deterioration of mechanical strength and crack evolution in rock specimens.

Author Contributions: S.Y.: Methodology, Formal analysis, Writing—review and editing, Writing—original draft; X.W.: Resources, Methodology, Writing—original draft, Data curation; Q.S.: Conceptualization, Methodology, Writing—review and editing; Z.W.: Visualization, Writing—original draft; G.T.: Investigation, Data curation, Software; G.Z.: Formal analysis, Funding acquisition; S.L.: Investigation, Data curation, Funding acquisition. All authors have read and agreed to the published version of the manuscript.

Funding: The research is financially supported by the Henan Provincial Science and Technology Research Project, China (NO. 242102320035, NO. 252102321113), and the High level Talents Project of North China University of Water Resources and Electric Power (NO. 202405005).

Data Availability Statement: Some or all data, models, or code that support the findings of this study are available from the corresponding author upon reasonable request.

Conflicts of Interest: Author Guantao Tai was employed by the company Henan No. 5 Geological Brigade Co., Ltd. The remaining authors declare that the research was conducted in the absence of any commercial or financial relationships that could be construed as a potential conflict of interest.

References

1. Schaefer, L.N.; Kendrick, J.E.; Oommen, T.; Lavallée, Y.; Chigna, G. Geomechanical rock properties of a basaltic volcano. *Front. Earth Sci.* **2015**, *3*, 29. [CrossRef]
2. Wang, S.Y.; Sloan, S.W.; Sheng, D.C.; Tang, C.A. Numerical analysis of the failure process around a circular opening in rock. *Comput. Geotech.* **2012**, *39*, 8–16. [CrossRef]
3. Leng, D.; Shi, W.; Liang, F.; Li, H.; Xiang, X.; Yan, L. Numerical analysis of the influence of dissolution pore structure on mechanical behavior of rock mass. *Comput. Part. Mech.* **2024**, *11*, 1695–1714. [CrossRef]

4. Yang, S.Q.; Huang, Y.H.; Tian, W.L.; Zhu, J.B. An experimental investigation on strength, deformation and crack evolution behavior of sandstone containing two oval flaws under uniaxial compression. *Eng. Geol.* **2017**, *217*, 35–48. [CrossRef]
5. Zhou, G.Q.; Yan, H.B.; Chen, K.H.; Zhang, R.T. Spatial analysis for susceptibility of second-time karst sinkholes: A case study of Jili village in Guangxi, China. *Comput. Geosci.* **2016**, *89*, 144–160. [CrossRef]
6. Wong, R.H.C.; Lin, P. Numerical study of stress distribution and crack coalescence mechanisms of a solid containing multiple holes. *Int. J. Rock Mech. Min. Sci.* **2015**, *79*, 41–54. [CrossRef]
7. Zeng, W.; Yang, S.Q.; Tian, W.L. Experimental and numerical investigation of brittle sandstone specimens containing different shapes of holes under uniaxial compression. *Eng. Fract. Mech.* **2018**, *200*, 430–450. [CrossRef]
8. Zhou, Z.; Tan, L.; Cao, W.; Zhou, Z.; Cai, X. Fracture evolution and failure behaviour of marble specimens containing rectangular cavities under uniaxial loading. *Eng. Fract. Mech.* **2017**, *184*, 183–201. [CrossRef]
9. Wong, R.H.C.; Lin, P.; Tang, C.A. Experimental and numerical study on splitting failure of brittle solids containing single pore under uniaxial compression. *Mech. Mater.* **2006**, *38*, 142–159. [CrossRef]
10. Zhao, C.; Matsuda, H.; Morita, C.; Shen, M.R. Study on failure characteristic of rock-like materials with an open-hole under uniaxial compression. *Strain* **2011**, *47*, 405–413. [CrossRef]
11. Chen, S.J.; Xia, Z.G.; Feng, F.; Yin, D.W. Numerical study on strength and failure characteristics of rock samples with different hole defects. *Bull. Eng. Geol. Environ.* **2021**, *80*, 1523–1540. [CrossRef]
12. Lin, Q.; Zhang, S.; Deng, H.; Shao, Z.; Liu, H.; Lan, M. Experimental and numerical studies of rock-like specimens with different hole shapes under compressive-shear loading. *Comput. Part. Mech.* **2025**, *12*, 889–905. [CrossRef]
13. Xia, Z.G.; Chen, S.J.; Liu, X.Z.; Sun, R. Strength characteristics and fracture evolution of rock with different shapes inclusions based on particle flow code. *Geomech. Eng.* **2020**, *22*, 461–473. [CrossRef]
14. Liu, H.; Liu, S.; Zhao, Y.; Wang, J.; Zheng, C.; Xia, Z.; Zheng, G. Numerical simulation of the effect of internal hole defect size on the mechanical properties of limestone. *PLoS ONE* **2022**, *17*, e0275626. [CrossRef] [PubMed]
15. Cui, C.; Wang, Q.C.; Ma, W.Q. Numerical investigation on the mechanical and stress characteristics of rock containing a spherical defect under uniaxial compression. *Comput. Part. Mech.* **2025**, *12*, 1507–1527. [CrossRef]
16. Liu, X.R.; Yang, S.Q.; Huang, Y.H.; Cheng, J.L. Experimental study on the strength and fracture mechanism of sandstone containing elliptical holes and fissures under uniaxial compression. *Eng. Fract. Mech.* **2019**, *205*, 205–217. [CrossRef]
17. Yang, S.Q.; Yin, P.F.; Zhang, Y.C.; Chen, M.; Zhou, X.P.; Jing, H.W.; Zhang, Q.Y. Failure behavior and crack evolution mechanism of a non-persistent jointed rock mass containing a circular hole. *Int. J. Rock Mech. Min. Sci.* **2022**, *114*, 101–121. [CrossRef]
18. Ma, W.B.; Chen, Y.L.; Yi, W.; Guo, S.C. Investigation on crack evolution behaviors and mechanism on rock-like specimen with two circular-holes under compression. *Theor. Appl. Fract. Mech.* **2022**, *118*, 103222. [CrossRef]
19. Du, M.R.; Jing, H.W.; Su, H.J.; Zhu, T.T.; Chen, M.L. Strength and failure characteristics of sandstone containing two circular holes filled with two types of inclusions under uniaxial compression. *J. Cent. South Univ.* **2017**, *24*, 2487–2495. [CrossRef]
20. Huang, Y.H.; Yang, S.Q.; Ranjith, P.G.; Zhao, J. Strength failure behavior and crack evolution mechanism of granite containing pre-existing non-coplanar holes: Experimental study and particle flow modeling. *Comput. Geotech.* **2017**, *88*, 182–198. [CrossRef]
21. Liu, H.; Liu, S.; Liu, H.; Fu, Y.; Kang, M.; Bai, Z.; Xu, J.; Zheng, C. Effect of the Number and Distribution of Circular Holes on the Damage and Fracture of Limestone Using PFC2D. *Geofluids* **2022**, *2022*, 9382577. [CrossRef]
22. Tang, C.A.; Wong, R.H.C.; Chau, K.T.; Lin, P. Modeling of compression-induced splitting failure in heterogeneous brittle porous solids. *Eng. Fract. Mech.* **2005**, *72*, 597–615. [CrossRef]
23. Huang, D.; Qiao, S.; Chang, X.; Wang, X.; Lu, H.; Pan, X. Study on macro–micro mechanical behavior of rock like samples with hole and cracks. *Comput. Part. Mech.* **2024**, *11*, 1579–1598. [CrossRef]
24. Li, Y.P.; Chen, L.Z.; Wang, Y.H. Experimental research on pre-cracked marble under compression. *Int. J. Solids Struct.* **2005**, *422*, 2505–2516. [CrossRef]
25. Yue, Z.; Zhou, J.; Feng, C.; Li, A.; Qiu, P.; Gang, M. Numerical investigation of the effect of holes on dynamic fracturing in multi-flawed granite. *Fatigue Fract. Eng. Mater. Struct.* **2021**, *44*, 1883–1896. [CrossRef]
26. Han, W.; Jiang, Y.; Luan, H.; Du, Y.; Zhu, Y.; Liu, J. Numerical investigation on the shear behavior of rock-like materials containing fissure-holes with FEM-CZM method. *Comput. Geotech.* **2020**, *125*, 103670. [CrossRef]
27. Lin, P.; Wong, R.H.C.; Tang, C.A. Experimental study of coalescence mechanisms and failure under uniaxial compression of granite containing multiple holes. *Int. J. Rock Mech. Min. Sci.* **2015**, *77*, 313–327. [CrossRef]
28. Milanović, P.T. The complexity of epikarst: Definitions and observations. *Carbonate Evaporites* **2025**, *40*, 127. [CrossRef]
29. Blatny, L.; Löwe, H.; Wang, S.; Gaume, J. Computational micromechanics of porous brittle solids. *Comput. Geotech.* **2021**, *140*, 104284. [CrossRef]
30. Huang, Y.H.; Yang, S.Q.; Tian, W.L. Cracking process of a granite specimen that contains multiple preexisting holes under uniaxial compression. *Fatigue Fract. Eng. Mater. Struct.* **2019**, *42*, 1341–1356. [CrossRef]
31. Gui, Y.L.; Zhao, Z.Y.; Zhang, C.; Ma, S.Q. Numerical investigation of the opening effect on the mechanical behaviours in rocks under uniaxial loading using hybrid continuum discrete element method. *Comput. Geotech.* **2017**, *90*, 55–72. [CrossRef]

32. Al-Harthi, A.A.; Al-Amri, R.M.; Shehata, W.M. The porosity and engineering properties of vesicular basalt in Saudi Arabia. *Eng. Geol.* **1999**, *54*, 313–320. [CrossRef]
33. Bubeck, A.; Walker, R.; Healy, D.; Dobbs, M.; Holwell, D. Pore geometry as a control on rock strength. *Earth Planet Sci. Lett.* **2017**, *457*, 38–48. [CrossRef]
34. Heap, M.J.; Xu, T.; Chen, C. The influence of porosity and vesicle size on the brittle strength of volcanic rocks and magma. *Bull. Volcanol.* **2014**, *76*, 856. [CrossRef]
35. Griffiths, L.; Heap, M.J.; Xu, T.; Chen, C.-F.; Baud, P. The influence of pore geometry and orientation on the strength and stiffness of porous rock. *J. Struct. Geol.* **2017**, *96*, 149–160. [CrossRef]
36. Lisjak, A.; Grasselli, G. A review of discrete modeling techniques for fracturing processes in discontinuous rock masses. *J. Rock Mech. Geotech. Eng.* **2014**, *6*, 301–314. [CrossRef]
37. Liu, S.; Liu, H.; Zhou, W.; Luo, J.; Feng, L.; Zhang, Z. Deformation response and failure characteristics of subgrade under varying dimensions and locations of hidden soil caves. *Eng. Fail. Anal.* **2025**, *178*, 109716. [CrossRef]
38. Bai, Q.S.; Tu, S.H.; Zhang, C. DEM investigation of the fracture mechanism of rock disc containing hole(s) and its influence on tensile strength. *Theor. Appl. Fract. Mech.* **2016**, *86*, 197–216. [CrossRef]
39. Liu, H.D.; Liu, S.; Xia, Z.G.; Liu, J.J.; Guo, H.; Yuan, Y.T. Study on mechanical properties and damage features of Rock-Coal-Rock combination models with defects and fillings. *Geomech. Eng.* **2021**, *27*, 239–251. [CrossRef]
40. Xia, Z.G.; Liu, S.; Bian, Z.; Song, J.; Feng, F.; Jiang, N. Mechanical Properties and Damage Characteristics of Coal-Rock Combination with Different Dip Angles. *KSCE J. Civil Eng.* **2021**, *25*, 1687–1699. [CrossRef]
41. Sarfarazi, V.; Saleh, A.A.; Fu, J.; Haeri, H.; Moez, M.T.; Moayer, A.; Golsanami, N. Experimental and numerical study of shear behavior of concrete-soft rock interface: With approach of concrete penetration in rock cavities. *Comput. Part. Mech.* **2025**, *12*, 327–349. [CrossRef]
42. Potyondy, D.O.; Cundall, P.A. A bonded-particle model for rock. *Int. J. Rock Mech. Min. Sci.* **2004**, *41*, 1329–1364. [CrossRef]
43. Pepe, G.; Mineo, S.; Pappalardo, G.; Cevasco, A. Relation between crack initiation-damage stress thresholds and failure strength of intact rock. *Bull. Eng. Geol. Environ.* **2017**, *77*, 709–724. [CrossRef]
44. Liu, S.; Liu, H.; Liu, H.; Xia, Z.; Zhao, Y.; Zhai, J. Numerical simulation of mesomechanical properties of limestone containing dissolved hole and persistent joint. *Theor. Appl. Fract. Mech.* **2022**, *122*, 103572. [CrossRef]
45. Rong, L.F.; Hu, J.L.; Li, H.R. Influence of defect hole location on acoustic emission characteristics and damage evolution of rocks: A numerical study based on particle flow code. *Comput. Part. Mech.* **2023**, *10*, 1943–1954. [CrossRef]
46. Zhou, J.; Zhang, L.; Peng, X.; Liu, H.; Jiang, R.H.; Zhang, L.Q.; Wang, S. Numerical study of voids geometry effects on sandstones mesoscopic fracture Mechanism: Insights from acoustic emission and moment tensor inversion. *Theor. Appl. Fract. Mech.* **2024**, *133*, 104588. [CrossRef]
47. Zhang, Z.K.; Lai, J.X.; Song, Z.P.; Xie, Y.L.; Qiu, J.L.; Cheng, Y.; Zhang, L. Investigating fracture response characteristics and fractal evolution laws of pre-holed hard rock using infrared radiation: Implications for construction of underground works. *Tunn. Undergr. Space Technol.* **2025**, *161*, 106594. [CrossRef]

Disclaimer/Publisher's Note: The statements, opinions and data contained in all publications are solely those of the individual author(s) and contributor(s) and not of MDPI and/or the editor(s). MDPI and/or the editor(s) disclaim responsibility for any injury to people or property resulting from any ideas, methods, instructions or products referred to in the content.